

## Chapter 4

### Copper Indium Gallium Diselenide: Photocurrent Generator

#### 4.0 Motivation, Objective, and Abstract

##### Motivation

CIGS technology has been escalated from cell to module by scaling up the deposition issues. Fabrication cost, process duration, an alternative to H<sub>2</sub>Se gas consumption, compositional uniformity, and heterojunction formation are always matter of concern. Light trapping management is also a key point of interest for yielding highly efficient CIGS devices. Reduced thickness of the CIGS layer and lightweight substrate is a foremost area of research.

##### Objective

- To fabricate CIGS sputter target for depositing CIGS thin-film layer by RF sputtering.
- To optimize the CIGS thin-film layer at different deposition pressure and RF power.
- To assess the effect of Rapid thermal annealing profiles on chalcopyrite CIGS phase formation.
- To evaluate the physical, optical, topographical, microstructural, elemental composition of the CIGS thin-film layer deposited at different deposition and annealing conditions.

##### Abstract

*Copper indium<sub>(1-x)</sub> Gallium<sub>(x)</sub> Diselenide (CIGS) layer for (x=0.3) was optimized for developing 50 x 50 mm CIGS solar cell module. For depositing the CIGS thin-film layer by RF-sputtering technique, single quaternary chalcopyrite CIGS sputter target was fabricated by cold press followed by a vacuum sintering process. CIGS thin-film layer has been deposited at 10, 15 and 20 mTorr deposition pressure and 125, 150 and 175 W RF-Power. The effect of Rapid thermal annealing was studied under different annealing*

*profiles. It was found that CIGS thin-film layer deposited at 15 mTorr, 150 W, and annealing for 250 °C results in a smooth surface however the grain size is very small. CIGS film-annealed under a two-step annealing process [400 °C (2 mins) + 550 °C (8 mins)] possess the sharp and intense X-ray peak. This confirms the increase in grain size as well as the phase conformation of CIGS chalcopyrite. Physical, optical, elemental, microstructural topographical analysis of CIGS thin-film was analyzed.*

#### **4.1 Chalcopyrite Absorber: CIGS Layer**

In the year 1975, the University of Maine (USA) achieved 4-5 % efficiency of small area CuInSe<sub>2</sub> solar cell by using dual-source evaporation (CuInSe<sub>2</sub> and Se<sub>2</sub>) technique [1]. W. E. Devaneg et.al from Boeing Aerospace and Electronics (USA) has introduced Ga in CuInSe<sub>2</sub> structure in the year 1990 [2]. They fabricated ZnO\CdZnS\CuInGaSe<sub>2</sub> solar cell and achieved 12.5 % efficiency under AM1.5 equivalent illumination for a total area of 1 cm<sup>2</sup> [3]. Since the year 1975, immense research has been made for achieving high efficiency of Copper Indium Gallium Diselenide (CIGS) solar cell. Presently, Solar Frontier has achieved 22.35 % of lab-scale efficiency of 1 cm<sup>2</sup>. Features like high optical absorption coefficient ( $\sim 10^5$  cm<sup>-1</sup>), tunable bandgap ( $\sim 1.15$  eV), long term stability, long diffusion of minority carrier have made CIGS a more fascinating absorber material over the past decades. For developing CIGS solar cell deposition techniques of two types 1. Vacuum process and 2. Non-Vacuum process. The most reliable, well established, and promising techniques for high-efficiency CIGS solar cell is 2-3 stages co-evaporation or multi-source evaporation. In this process, single or binary, or ternary precursors are deposited at substrate temperature and then the excess of Se is supply is provided at 3 stage. This technique has attracted many PV industries due to its high success rate, but it has demerits of high production cost, process complexity, and variation in stoichiometric compositions. Other techniques like sputtering, MOCVD, MBE, Sol-gel, spray pyrolysis, electrochemical deposition, etc., are widely adopted techniques but still some key challenges for capturing the PV market. Challenges such as production cost, material availability, stability, toxicity, elemental composition, defects formation, excess Se supply (in

absorber layer), and lab to module efficiency are still under debate. The pseudobinary phase diagram of the CIGS chalcopyrite phase is shown in Fig. 4.1. The chalcopyrite is stable from room temperature to 810 °C and such phase without the presence of additionally binary phases when Cu content is of 24-24.5 % [4].

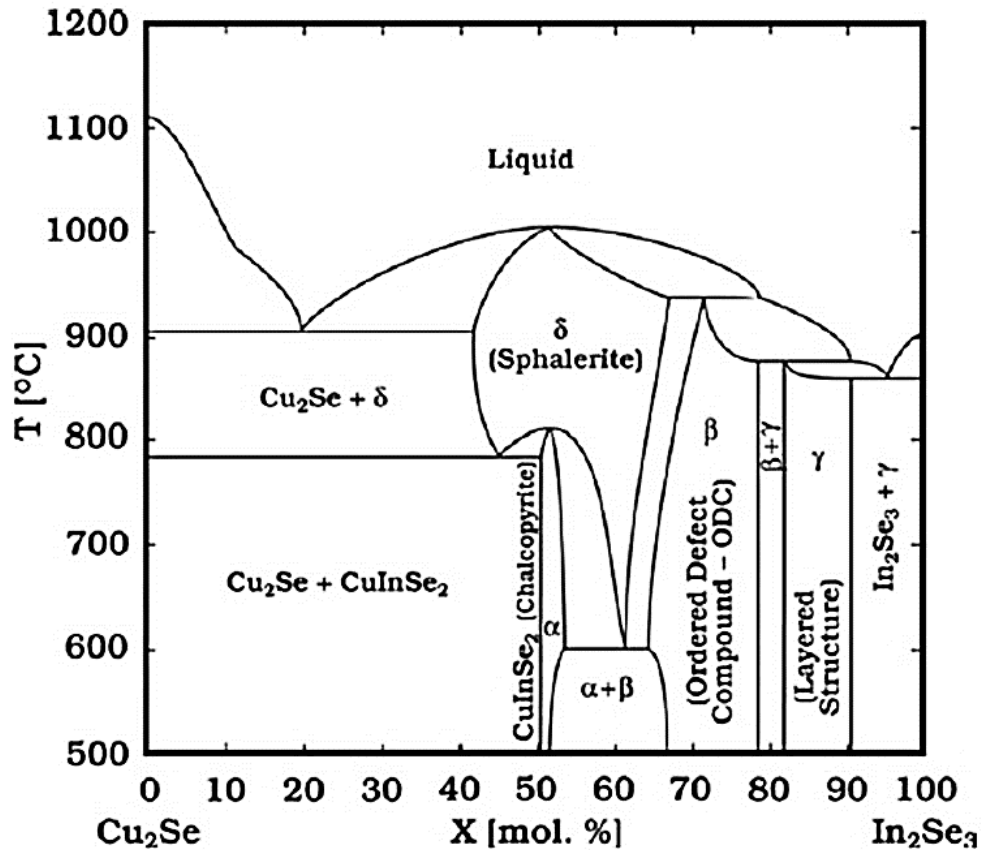
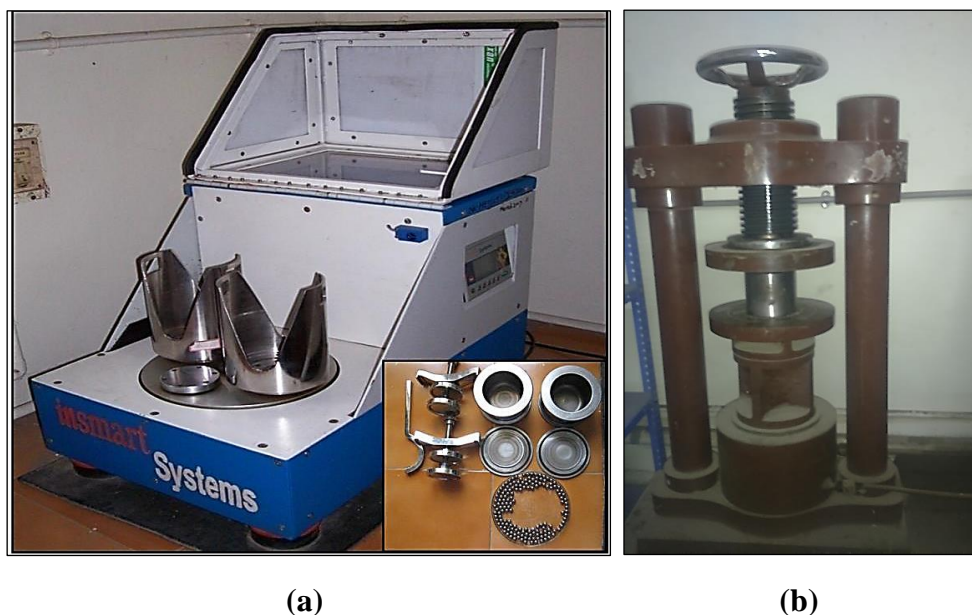


Fig: 4.1: Pseudobinary phase diagram of Chalcopyrite CIGS phase.

## 4.2 Experimental Details

High energy ball milling in a twin bowl planetary ball mill system is used to form CIGS bulk powder. Raw materials were in powder form and weighed in their stoichiometric compositions, that is 1:0.7:0.3:2. The raw materials were preliminary hand-mixed in the jar. The twin ball planetary system (M/s. Insmart System, Hyderabad) of 250 ml in capacity were operated at 400 rpm with the ball to powder ratio of 10:1, in an argon environment for 2.5 hours shown in Fig. 4.2 (a). The green compact has formed using the cold press technique

shown in Fig. 4.2 (b) in a die of 1 inch in diameter. Further, vacuum sintering of green compact at 500 °C for one hour was performed to form the CIGS target.



**Fig. 4.2: Image of (a) Twin bowl planetary ball mill system (M/s. Insmart System, Hyderabad), and (b) Cold Press Machine.**

The CIGS target has been fabricated using high energy ball milling followed by cold pressing and vacuum sintering process. Fig. 4.3 shows the optical images of ball-milled CIGS powder 4.3 (a), green compact of CIGS target 4.3 (b) and finally vacuum sintered CIGS target 4.3 (c).

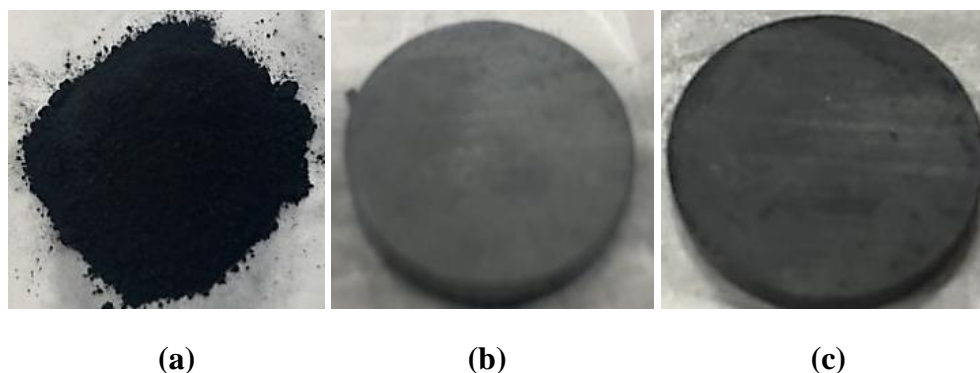


**Fig. 4.3: Optical image (a) Ball milled CIGS powder and (b) Cold press (c) Vacuum sintered CIGS target at 500 °C for one hour.**

This target was used to prepare a CIGS thin film on a 60 x 60 x 1 mm SLG substrate using RF sputtering technique. Variable deposition conditions i. e., deposition pressure (10, 15, and 20 mTorr), RF power (125, 150, and 175 W),

and annealing temperature (150, 200, and 250 ° C) were adopted to optimize the formation of chalcopyrite phase. Argon flow was kept at 6 sccm and source to substrate distance was 5 cm. Several characterizations such as phase conformations, topography, optical, elemental composition analysis, Raman spectroscopy, photoluminescence spectra were carried out to study the physical and optoelectronic properties of CIGS thin film.

## 4.3 Results and Discussion

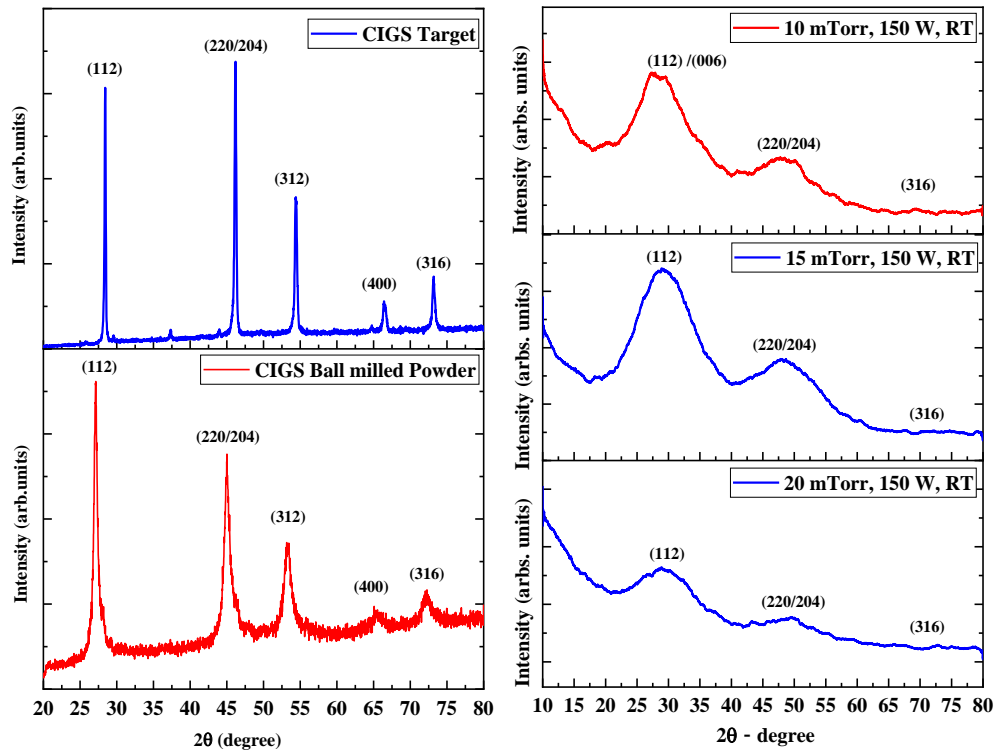
### 4.3.1 X-Ray Diffraction Analysis

Phase conformation analysis of chalcopyrite CIGS tetragonal structure has been carried out. X-Ray Diffraction (XRD) analysis of High Energy Ball milled CIGS powder, vacuum sintered CIGS target and RF sputtered CIGS thin films deposited at different pressure (10, 15, and 20 mTorr), RF power (125, 150, and 175 W) at room temperature and vacuum annealing for one hour (150, 200 and 250 °C). In Fig. 4.4 (a), both high energy ball milled CIGS powder and CIGS vacuum sintered target possess major peaks at  $2\theta$  value 26.96 ° and 27.07 ° having phase with  $(hkl)$  value  $(112)$ . Other phases at  $(220/204)$ ,  $(312)$ ,  $(400)$  and  $(316)$  were also present in both CIGS powder at  $2\theta$  value 44.98 °, 53.28 °, 65.38 °, 72.24 ° as well as CIGS target at 46.18 °, 54.44 °, 66.38 °, and 73.16 °. One very small peak at  $2\theta$  value 37.4 ° having  $(hkl)$  value  $(211)$  is also present which confirms the chalcopyrite phase formation. These results have been confirmed with JCPDS card no. 35-1102 [5]. No other peak of binary, ternary composite or any elements were observed. This CIGS powder was prepared using a mechano-chemistry technique which is a conventional method to avoid the toxic and high-temperature process. In high energy ball milling technique, elements undergo fracturing, re-welding, and cold- welding of particles. Due to these, granules of In, Ga, and Se and powder Cu diffuse into each other and undergo a self-propagating high-temperature synthesis process.

Besides, BPR 10:1 and rotation speed 400 rpm found appropriate for CIGS chalcopyrite phase formation. Inhomogeneity in CIGS alloy can be caused due to low rotation speed which increases milling time and less time available for the diffusion of elements into each other [6]. In the case of high rotation speed,

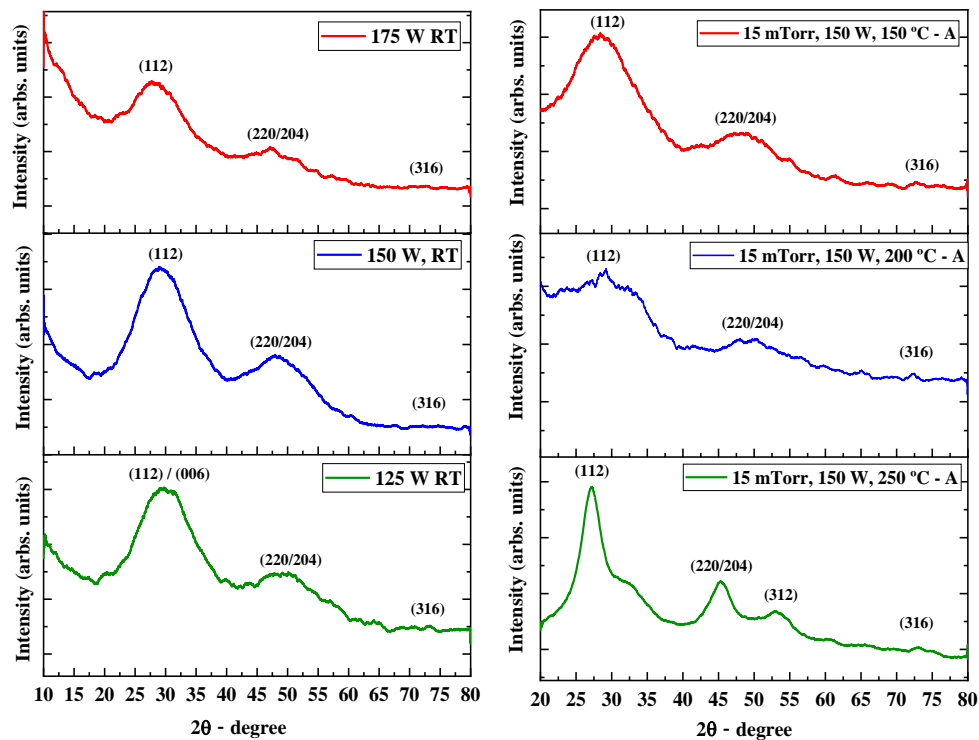
excessive heat energy is generated which may form other binary or ternary phases. Compared to CIGS powder, vacuum sintered CIGS target has more sharp and intense peaks due to dense and compact CIGS target formed 500 °C. This vacuum sintering temperature promotes the growth of crystallites by reducing grain boundaries. There may be selenium loss because the sintering temperature is high compared to the evaporation temperature of Se. This may lead to the low relative density of the target. For a high-quality sputtering target about 92 % of relative density is recommended. In our vacuum sintered CIGS target relative density of 73.14 % was obtained [7, 8]. Fig. 4.4 (b) represent XRD spectra of CIGS thin-film deposited at variable pressure (10, 15, and 20 mTorr) at constant RF power 150 W. At 15 mTorr deposition pressure, major peak at (*112*) with  $2\theta$  value 28.65 °. Double peak s one at  $2\theta$  value 27.28 ° and another at 29.64 ° was observed. This shows that at 10 mTorr not only CIGS but other phases such as Cu<sub>2</sub>Se or GaSe may present. No change was observed for CIGS thin-film deposited at 20 mTorr. The (*112*) peak was less intense which confirms the poor crystallinity of the CIGS phase. In Fig 4.4 (c), CIGS thin-film deposited at RF power 150 W has an intense major peak of (*112*) phase at  $2\theta$  value 28.02 °; while at 125 and 175 W RF power CIGS thin films show poor crystallinity. At 125 W due to the difference in vapor pressure, the kinetic energy of each element allows forming the CIGS phase with other binary phases such as CuSe, Cu<sub>2-x</sub>Se, Cu<sub>2</sub>Se. On another hand, at 175 W RF power again the intensity of major peak decrease and get broader with an increase in RF power may lead to re-sputtering of elements or modification in stoichiometric composition, further forming binary composition [9]. The effect of 1-hour vacuum annealing on CIGS thin films deposited at 15 mTorr and 150 W RF power is shown in Fig. 4.4 (d). At 150 °C, no change was observed in XRD spectra as shown in Fig. 4.1 (d) compared to CIGS thin-film deposited at 15 mTorr at room temperature. Suddenly on increasing annealing temperature to 200 °C CIGS phase was not detectable. At 200 °C, no sharp peak of CIGS chalcopyrite was observed. Probably, CuSe, Cu<sub>2-x</sub>Se, Cu<sub>2</sub>Se,  $\gamma$ -(In, Ga)<sub>2</sub>Se<sub>3</sub> (JCPDS-40-1407),  $\beta$ -(In, Ga)<sub>2</sub>Se<sub>3</sub> (JCPDS-40-1408) and Cu (In, Ga)<sub>3</sub>Se<sub>5</sub> ( $\beta$ -CIGS) phases were found. These intermediate phases formed due to Cu diffusion out from the CIGS phase and intermixing of metal alloy compound. On increasing annealing temperature to 250 °C, a sharp CIGS phase was

observed confirming the CIGS chalcopyrite phase. No other binary phase such as CuSe, Cu<sub>2-x</sub>Se, Cu<sub>2</sub>Se, In<sub>2</sub>Se<sub>3</sub>, etc. was observed. But Cu (In, Ga)<sub>3</sub>Se<sub>5</sub> ( $\beta$ -CIGS) still present which is still indistinguishable from the CIGS phase.



(a)

(b)



(c)

(d)

**Fig. 4.4: XRD spectra of (a) Ball milled CIGS powder and CIGS target; CIGS thin films deposited at various (b) pressure, (c) RF power, and (d) annealing under vacuum environment.**

### **4.3.2 X-Ray Fluorescence Analysis**

Stoichiometric elemental composition for high energy ball milled CIGS powder, vacuum sintered CIGS target, and CIGS thin-film deposited at various conditions was measured using X-Ray Fluorescence technique mentioned in Table 4.1. For achieving high efficiency CIGS solar cell, stoichiometric composition of CIGS thin-film should maintain to Cu:In:Ga:Se = 1:0.7:0.3:2 i. e.  $Cu/(In+Ga) = 1.0$ ,  $Ga/(Ga+In) = 0.3$  and  $Se/(Cu+Ga+In) = 1.0$ . A slight deviation from stoichiometric composition will result in poor performance of CIGS solar cells. For 10 mTorr, Cu and Se content were found more due to which the  $Cu/(In+Ga)$  ratio is 1.38, and  $Se/(Cu+Ga+In)$  is 1.12. Similar results were obtained for CIGS thin-film deposited at 20 mTorr. This confirms the stoichiometric deviation in CIGS thin films, but at 15 mTorr  $Cu/(In+Ga) = 1.15$  and  $Ga/(Ga+In) = 0.30$  was well maintained. There was a slight increment in Cu and Se content, but still result was good in agreement to the which indicates the presence of all elements in the stoichiometric composition. As such no Se deficient was observed for CIGS thin-film deposited at different pressure, this indicates that there might be the formation of phases CuSe,  $Cu_{2-x}Se$ ,  $Cu_2Se$ ,  $Ga_2Se_3$ . RF power affects the stoichiometric composition of CIGS thin films. At 125 W RF power  $Cu/(In+Ga) = 1.17$ , while  $Ga/(Ga+In) = 0.30$  and  $Se/(Cu+Ga+In) = 1.06$ ; here proper diffusion of Cu, In, Ga, and Se atoms forming CIGS phase. Only atoms might have reached the substrate surface but still have high surface energy for the homogenous CIGS phase. On increasing RF power to 175 W, a decrease in Se and In content was observed. Due to the high vapor pressure of Se, it gets volatile or it may undergo re-sputtering of atoms. But 150 W, RF power no deviation in stoichiometric composition i. e.  $Cu/(In+Ga) = 1.02$ ,  $Ga/(Ga+In) = 0.30$  and  $Se/(Cu+Ga+In) = 1.06$  was observed. Annealing is a widely accepted process for improving crystallinity, homogeneity, grain size, and maintaining the stoichiometric composition of an absorber. CIGS thin-film annealed at 250 °C under a vacuum environment for

1 hour has nearly no deviation in the stoichiometric composition. Slight Cu/(In+Ga) was more 1.13. In comparison to 250 °C annealing temperature, CIGS thin-film annealed at 150 and 200 °C also slight deviation [13]. But this deviation has more impact due to the formation of different binary phases such as CuSe, Cu<sub>2-x</sub>Se, Cu<sub>2</sub>Se, Ga<sub>2</sub>Se<sub>3</sub>, etc., which has been confirmed from XRD reports. One more important thing that has been noticed here that Se loss is very negligible compared to other deposition techniques such as co-evaporation 2-3 stages and annealing. Therefore, one step sputtering of CIGS thin films from a single CIGS chalcopyrite target is benefitted is reducing the number of sputtering components of different elemental or binary or ternary materials and use of excess Se content.

**Table 4.1: Elemental Composition of all CIGS thin film deposited at various deposition parameters.**

Parameters		Cu (at%)	In (at%)	Ga (at%)	Se (at%)	Cu/ (In+Ga)	Ga/ (In+Ga)	Se/ (Cu+In+Ga)
10 mTorr	150 W, RT	27.31	12.95	6.76	52.96	1.385	0.342	1.125
15 mTorr		26.55	16.00	6.98	50.46	1.155	0.303	1.018
20 mTorr		28.24	13.85	6.96	50.93	1.356	0.334	1.038
125 W	15 mTorr, RT	26.08	15.59	6.69	51.62	1.170	0.300	1.067
150 W		26.30	18.45	7.18	48.06	1.026	0.280	0.925
175 W		27.26	17.66	6.82	48.25	1.113	0.278	0.932
150 °C - Annealed	15 mTorr, 150 W	27.40	15.5	6.97	50.13	1.219	0.310	1.005
200 °C - Annealed		26.96	15.88	6.58	50.57	1.200	0.293	1.023
250 °C - Annealed		26.31	16.30	6.79	50.58	1.139	0.294	1.023

### 4.3.3 Raman Spectroscopic Analysis

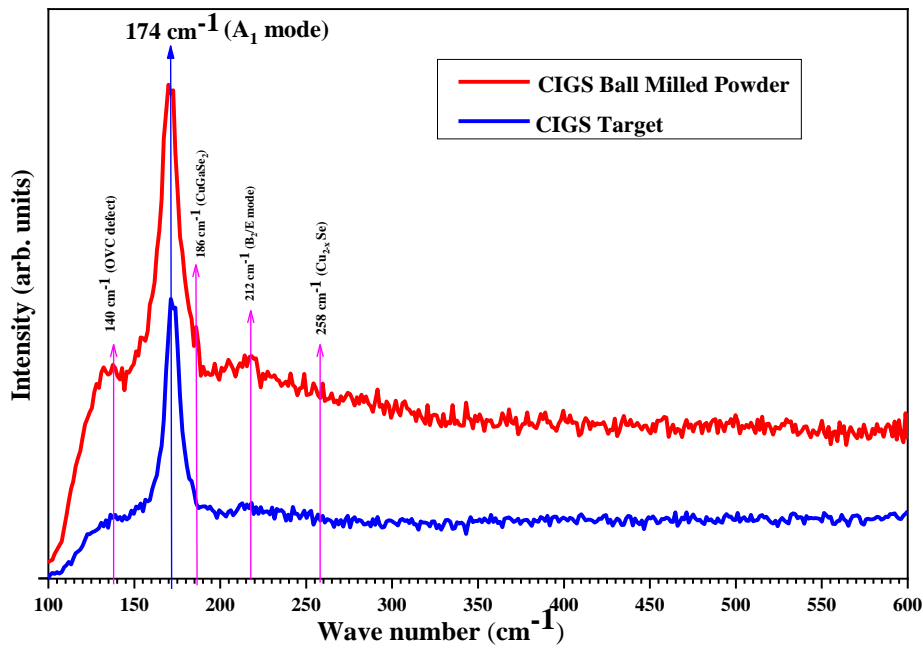
For a detailed analysis of phase conformation and quality of crystallinity, Raman spectroscopy is a novel technique. A quaternary phase CIGS belongs to the characteristic of  $A^I B^{III} C_2^{VI}$  chalcopyrite compound which has the strongest primary  $A_1$  mode peak centered at  $175\text{ cm}^{-1}$ . Other secondary mode  $B_1$ ,  $B_2$ , and E scattering peaks are weak and broad within the  $210\text{-}220\text{ cm}^{-1}$  range. Fig. 4.5 (a) represents Raman spectra of high energy ball milled CIGS powder and in-house vacuum sintered CIGS target. Both show an  $A_1$  mode peak at  $174\text{ cm}^{-1}$  which confirms the presence and formation of the CIGS phase [14]. Also, another shoulder peak at  $140\text{ cm}^{-1}$  was observed strongly for CIGS ball milled powder but it was suppressed for the CIGS target. This peak depicts ordered vacancy defects (OVC). CIGS target has a much dense compact structure compare to CIGS powder. Secondary mode ( $B_2/E$ ) was also present at a peak of  $212\text{ cm}^{-1}$ . A ternary phase ( $\text{CuGaSe}_2$ ) at  $180\text{ cm}^{-1}$  was suspected of CIGS powder only and no other phases  $\text{CuSe}$ ,  $\text{Cu}_{2-x}\text{Se}$ ,  $\text{Cu}_2\text{Se}$ , and  $\text{Ga}_2\text{Se}_3$  were detected. From the results, it is inferred that using high energy ball milling technique and vacuum sintering  $500\text{ }^\circ\text{C}$  for a 1hour chalcopyrite CIGS phase with no other binary phase can be obtained. Fig. 4.5 (b) shows Raman spectra for CIGS thin-film deposited at various pressure.  $A_1$  mode peak at  $175.58\text{ cm}^{-1}$  for 15 mTorr,  $173.00\text{ cm}^{-1}$  for 10 mTorr, and  $176.10\text{ cm}^{-1}$  for 20 mTorr were observed which shows the presence of CIGS chalcopyrite phase. Also, a strong peak except for 15 mTorr at  $257.73\text{ cm}^{-1}$  for 10 mTorr and  $258.79\text{ cm}^{-1}$  for 20 mTorr was detected and only the CIGS phase was present at 15 mTorr. These peaks resemble the formation of binary phases  $\text{CuSe}$ ,  $\text{Cu}_{2-x}\text{Se}$ ,  $\text{Cu}_2\text{Se}$ . From XRD analysis, it was difficult to separate the chalcopyrite and binary phase, therefore using Raman spectroscopy they can be easily detectable. For CIGS thin film deposited at various RF power is shown in Fig. 4.5 (c).  $A_1$  mode peak  $175.98\text{ cm}^{-1}$  for 125 W,  $175.07\text{ cm}^{-1}$  for 150 W and  $171.96\text{ cm}^{-1}$  for 175 W as well as binary phase at peak  $258.28\text{ cm}^{-1}$  for 125 W and  $253.17\text{ cm}^{-1}$  for 175 W was observed. These results are in accordance with CIGS thin-film deposited at variable pressure i. e. only at 150 W pure CIGS phase has formed with no other binary phase. At 150 and  $250\text{ }^\circ\text{C}$ , only  $A_1$  mode peak at  $174.55$  and  $175.69\text{ cm}^{-1}$  were observed with no other binary phase [15]. Still, peaks were broad due to insufficient improvement in crystallinity and a slight excess amount of Cu content. But at  $200\text{ }^\circ\text{C}$ ,  $A_1$  mode for the CIGS phase was completely absent, a

sharp peak of CuSe or Cu<sub>2-x</sub>Se was present. One of the reasons may be the diffusion of Cu atoms along large grain boundaries and with Se atoms too. A shift in the CIGS chalcopyrite phase can be estimated according to the report of Roy. et al. [16] equation (4.1) mentioned below,

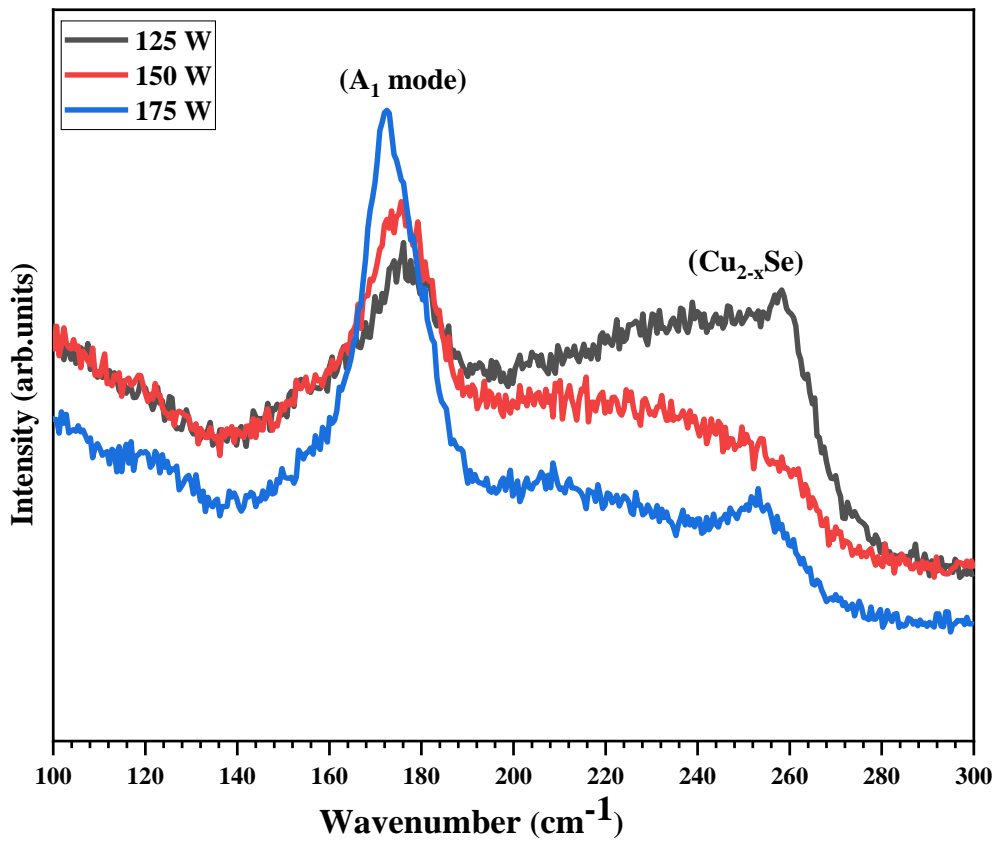
$$F = 173 + 12.92(x) \quad (4.1)$$

Where F = Raman frequency and (x) = Ga/(Ga+In).

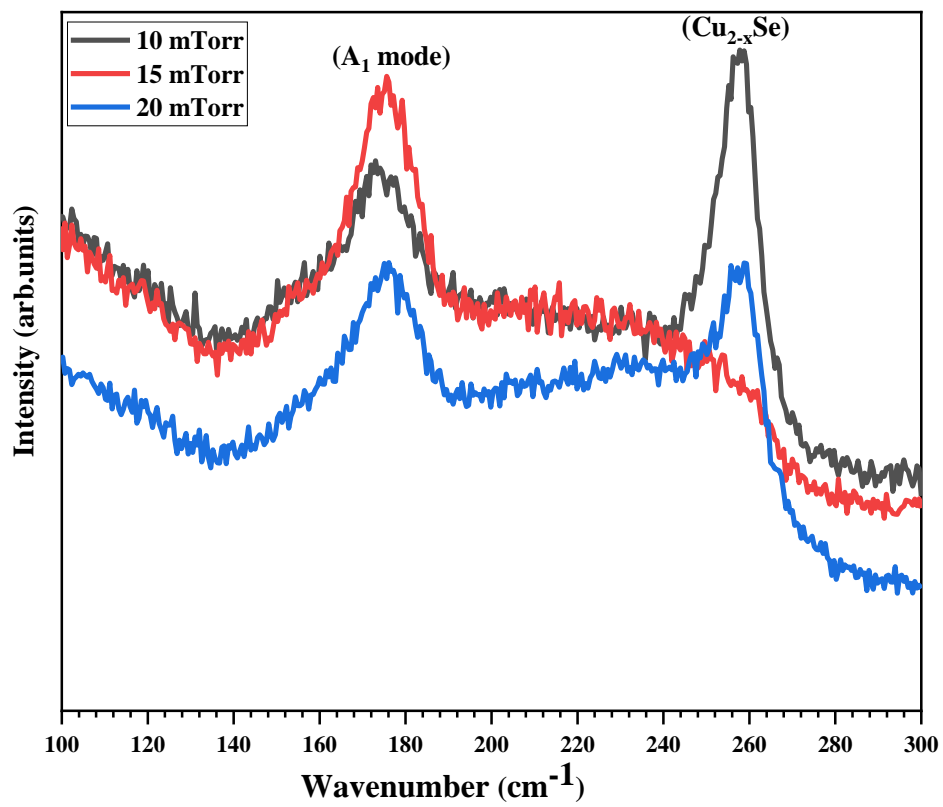
One of the main causes of Raman shift is Ga/(Ga+In) ratio. As Ga atoms are substituted for In atoms, bond length at the lattice site is modified. The bond length gets larger due to the gallium's low ionic radius. Depending upon Cu content defects and binary Copper Selenide phases are formed. In the case of Cu-poor thin films, the OVC defects phase in a random way can be easily introduced in the form of lattice complex defects such as antisite In<sub>Cu</sub> and V<sub>se</sub><sup>-2</sup> 2VCu<sup>-2</sup> vacancies and Cu (In Ga)<sub>3</sub>Se<sub>5</sub> or Cu<sub>2</sub>(In Ga)<sub>4</sub>Se<sub>7</sub> phases are formed. Meanwhile, Cu-rich films show the formation of CuSe, Cu<sub>2-x</sub>Se, and Cu<sub>2</sub>Se phases. The shift in vibration mode also may be due to local stress developed during various deposition conditions. Regardless, sputtering from single quaternary CIGS target results only in A<sub>1</sub> mode vibration, no other weak mode B<sub>1</sub>/E, and B<sub>2</sub>/E nor any secondary defect phases.



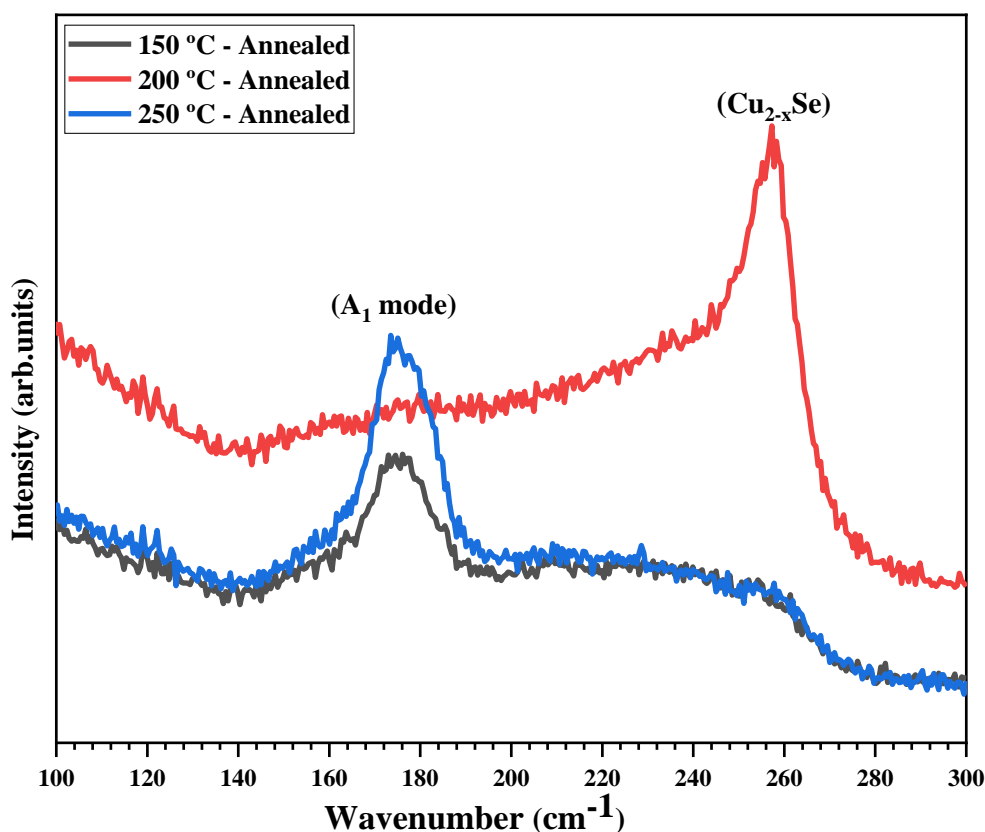
(a)



(b)



(c)



(d)

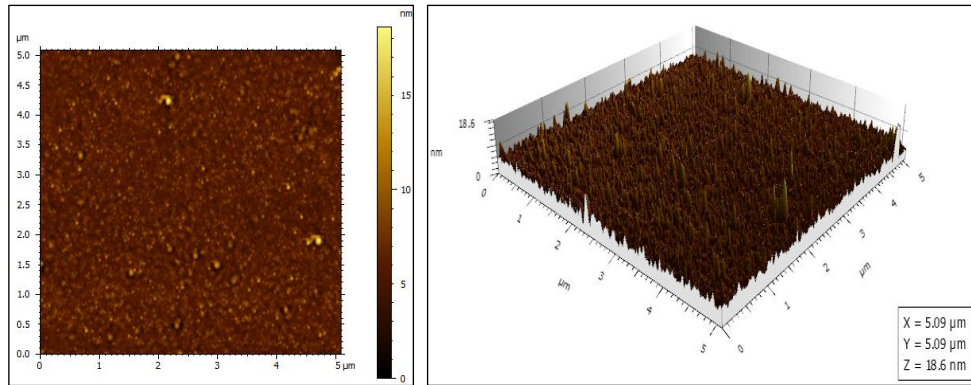
**Fig. 4.5: XRD spectra of (a) Ball milled CIGS powder and CIGS target, CIGS thin films deposited at various (b) pressure, (c) RF power, and (d) annealing under vacuum environment.**

#### 4.3.4 Atomic Force Microscopic Analysis

To investigate topographical changes in CIGS thin-film due to variable deposition conditions, the AFM technique is used. 2D and 3D topographical of CIGS thin-film are shown in Fig. 4.6. CIGS thin-film deposited at 10 mTorr, possess conical rod texture as shown in Fig. 4.6 (a and b). The growth is uniform but conical rods are separated apart distances. The root means square roughness (Rrms) value is 7.704 nm. The surface has a rough texture which is due to the shadowing effect. When sputtered particles approach the substrate surface not at a normal angle but with an oblique angle then particles are capture by higher surface points forming hills. Here conical rods are thin in dimension due to the re-sputtering process [17, 18]. The flux of incident particles has a low sticking coefficient, and they are knocked off by incoming energetic atoms at 10 mTorr. The re-sputtering process is followed by the re-deposition process on the

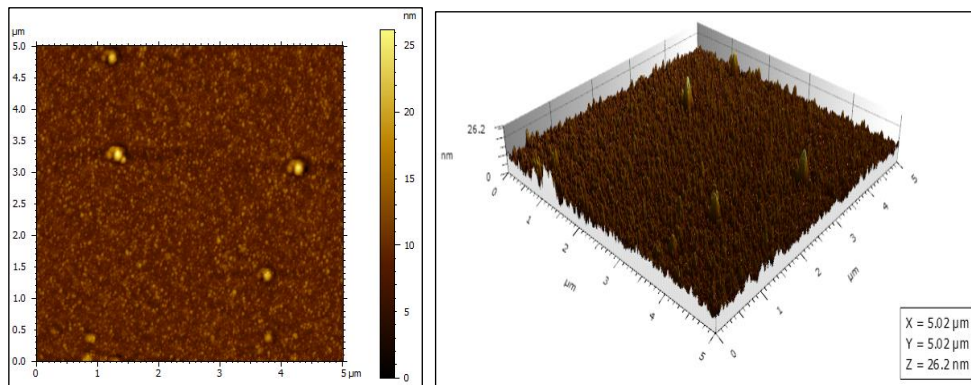
surface. At 15 mTorr, the surface roughness value decreases to 1.736 nm. Decrease in surface roughness due to homogenous deposition of incident particles flux. Besides, an amalgamation of incident flux forming large hillock texture also took place as shown in Fig. 4.6 (c and d). Further on increasing deposition pressure to 20 mTorr, surface texture has transformed from conical rods to rough lumps shown in Fig. 4.6 (e and f). Probably, due to increasing pressure more collision between  $\text{Ar}^+$  ions and sputtered atoms take place which reduces the kinetic energy of incident particles reaching to substrate surface. Particles reach to the substrate to arrange themselves rather than undergoing the re-sputtering process. This increased surface roughness value to 3.442 nm. The impact of change in RF power has an insignificant change in the texture of the deposited CIGS thin film. At 125 W, sputtered particles have formed few large conical dome textures and due to low sticking coefficient particles have re-sputtered forming granules texture as shown in Fig. 4.6 (g and h). Due to the insufficient energy of sputtered atoms, there is inhomogeneity in the formation of conical dome texture. This leads to increase roughness to 5.560 nm. But conical dome texture modified into homogenous conical rods which reduce surface roughness to 1.698 nm at 150 W RF power as shown in Fig. 4.6 (i and j). These conical rods disappear on increasing RF power to 175 W. A mixture of the conical dome and globule texture has appeared as showing in Fig. 4.6 (k and l). In addition, partial film texture appeared to be smooth. Due to a mixture of two different textures, surface roughness to 5.086 nm increased. Vacuum annealing of CIGS thin-film intends to improve crystallinity and grain size. Annealing CIGS thin-film at 150 °C, the surface texture is comprised of irregular aggregates forming rough surfaces due to which surface roughness  $R_{\text{rms}}$  was 6.735 nm as shown in Fig. 4.6 (m and n). At 150 °C, due to lattice sites rearrangement modification in texture takes place. Conical rods at RT tends to become irregular rough aggregates. Surprisingly, annealing CIGS thin-film at 200 °C has a triangular conical with very few small rough lumps texture as shown in Fig. 4.6 (o and p). More likely, the film has a very smooth texture comprise of nanocrystals. The surface roughness slightly decreases to 5.084 nm. Finally, at 250 °C annealing temperature surface texture comprise of few larger rough lumps as well as conical dome textured crystallites amalgamate to form substantial crystallites as shown in Fig. 4.6 (q and r). This reduces the surface

roughness to 2.787 nm. It was apparent from the topographical analysis that CIGS thin-film having CuSe or Cu<sub>2-x</sub>Se phase has a smooth texture compared to chalcopyrite CIGS with rough surface texture.



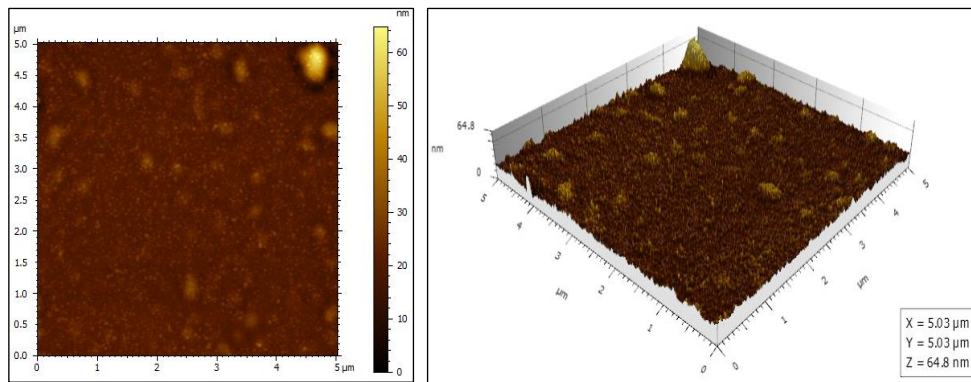
(a)

(b)



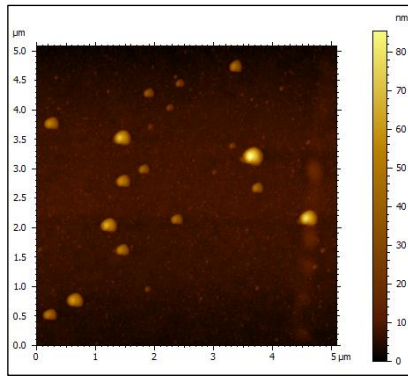
(c)

(d)

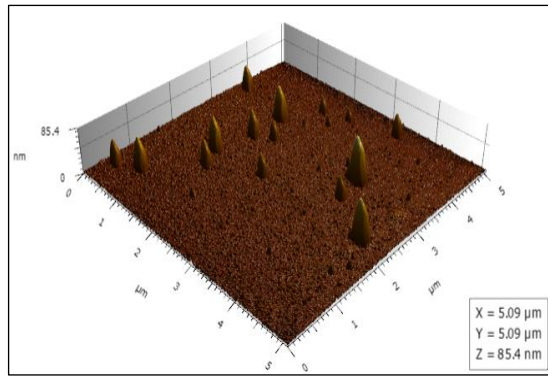


(e)

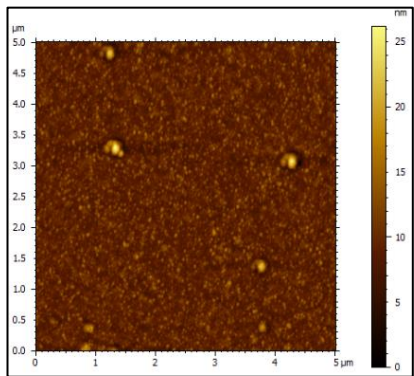
(f)



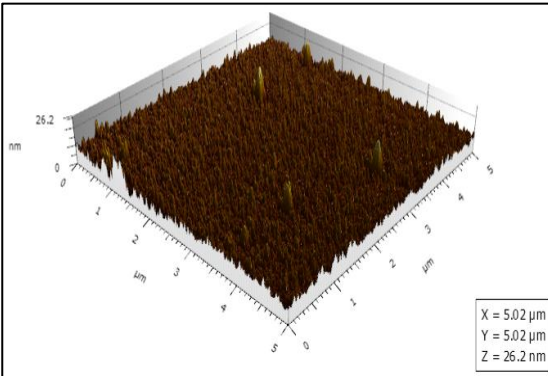
**(g)**



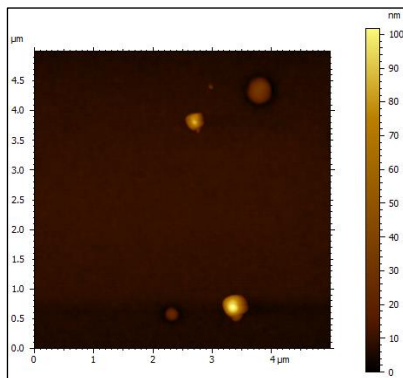
**(h)**



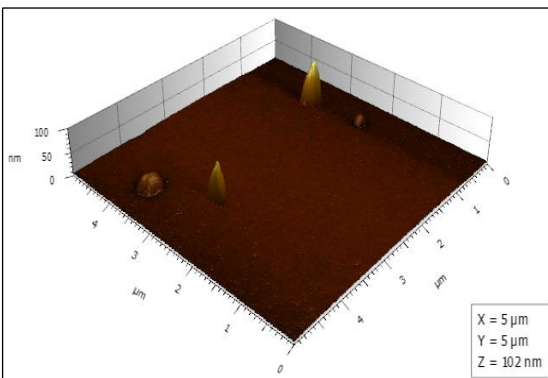
**(i)**



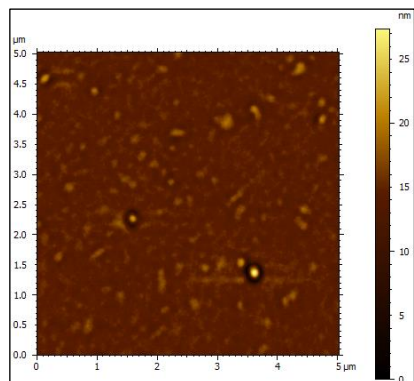
**(j)**



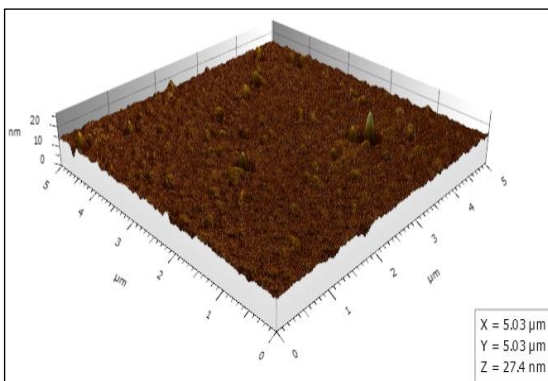
**(k)**



**(l)**



**(m)**



**(n)**

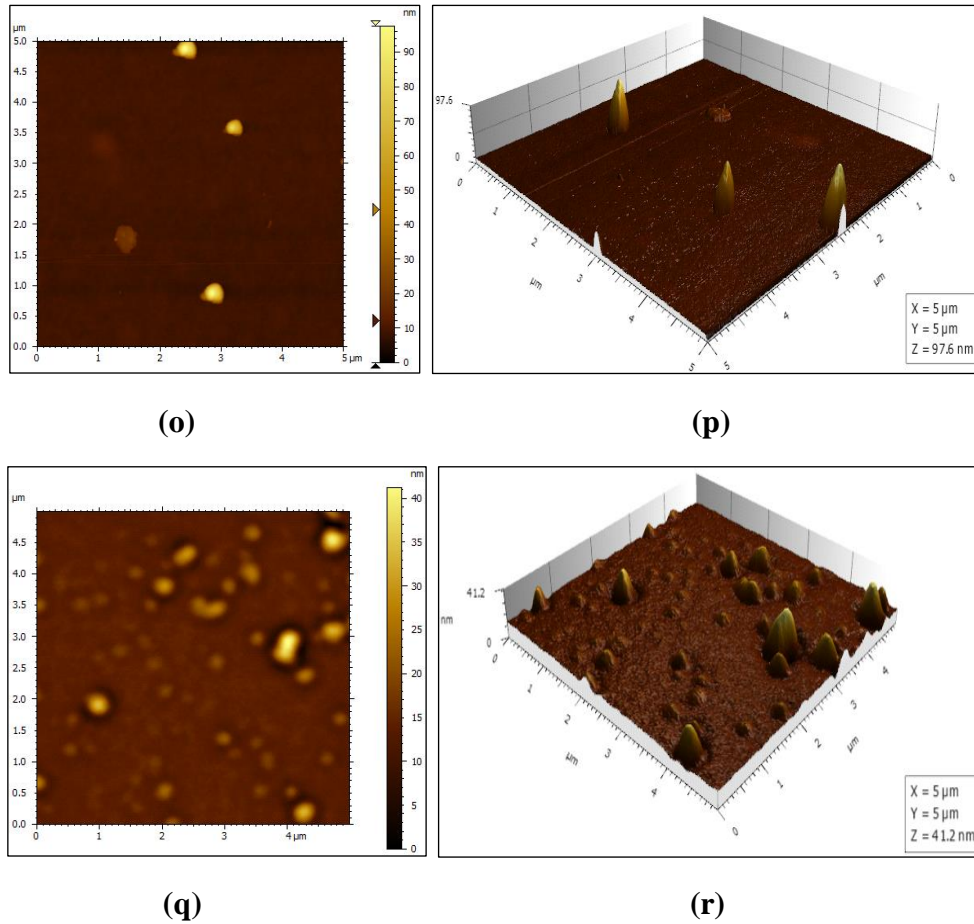


**Fig. 4.6: 2D and 3D topographical (AFM) images of CIGS thin films deposited at various (a) pressure [10 mTorr (a, b), 15 mTorr (c, d), and 20 mTorr (e, f)], (b) RF power [125 W (g, h), 150 W (i, j), and 175 W (k, l)], and (c) annealing [150 °C (m, n), 200 °C (o, p), and 250 °C (q, r)] under vacuum environment.**

### 4.3.5 Microstructural Analysis

Microstructural images of CIGS thin-film deposited under different deposition conditions are shown in Fig. 4.7. At 10 mTorr shown in Fig. 4.7 (a), spherular morphology of mixed metalloids phases has appeared. Increasing pressure to 15 mTorr, spherules are transformed into channels. Still, few spherules are present on the surface as shown in Fig. 4.7 (b). This confirms that not pure crystalline CIGS has formed; partially other mixed phases are also present. At 20 mTorr, similar spherules like 10 mTorr appeared on the surface as shown in Fig. 4.7 (c). Scanning electron microscopic image as shown in Fig. 4.7 (d), (e), and (f) reveals the change in the contour of the morphology as the deposition power

varies 125, 150, and 175 W. Imprecise coarse grains are formed at RF power 125 and 175 W. Also, circular agglomeration of metalloids phase like ( $\text{Cu}_2\text{Se}$ ) was observed. This phase has been confirmed with XRD and Raman spectroscopic analysis. Whereas, at 150 W no such secondary phase is reflected in morphology. It was noticed that spherules approach to diffuse into channels to form conformal coverage over the surface. Annealing for one hour at constant temperature resulted in coarse grain formation. At 150 °C shown in Fig. 4.7 (g) and at 200 °C shown in Fig. 4.7 (h), irregularly shaped grains have formed. As such no significant metamorphose was observed. Segregated metalloids diffused among each other at annealing temperature 250 °C shown in Fig. 4.7 (i), mutating to form a nearly smooth surface with a single chalcopyrite phase with negligible binary phases [19].

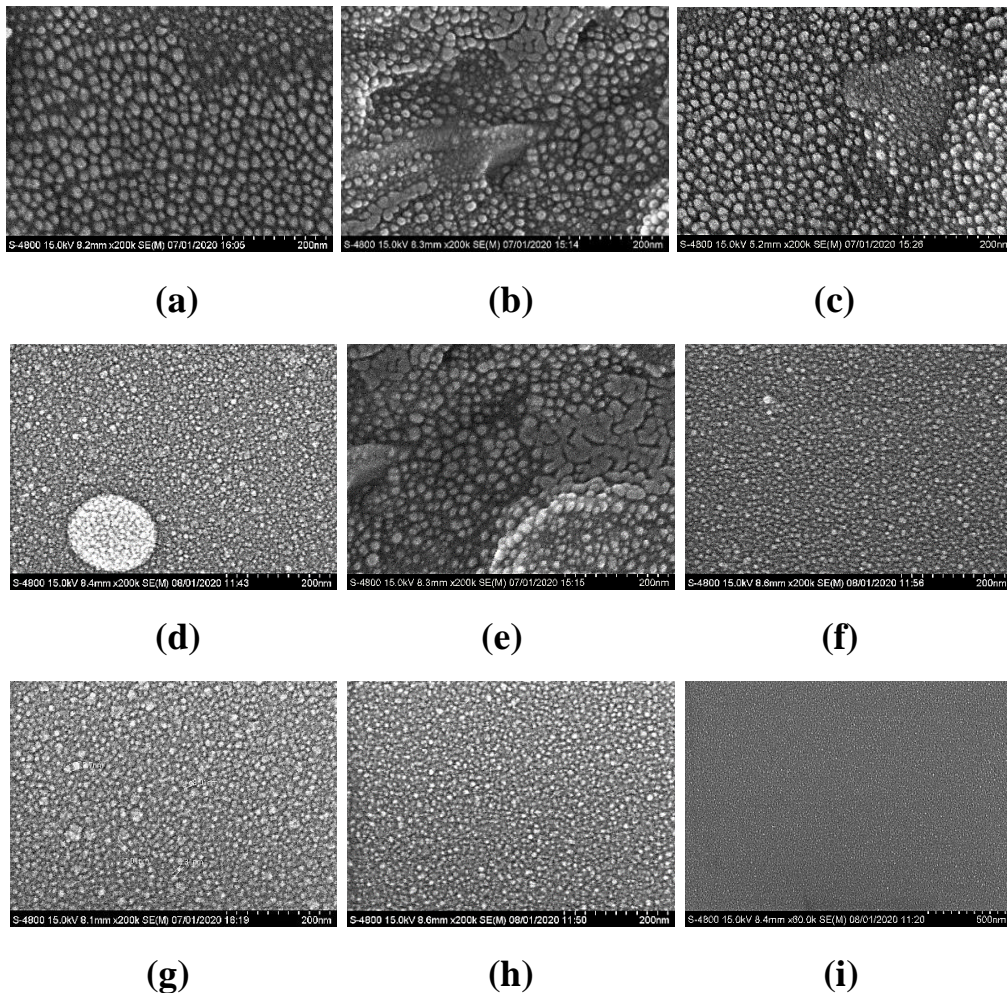


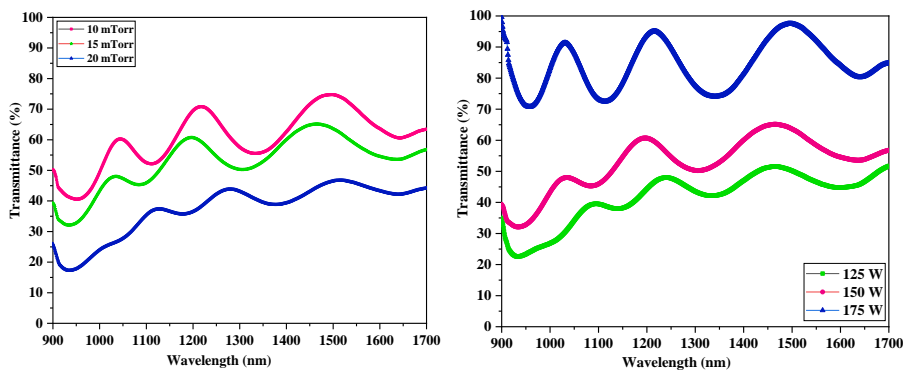
**Fig. 4.7: Scanning Electron Microscopic images of CIGS thin films deposited at various (a) pressure [10 mTorr-(a), 15 mTorr-(b), and 20 mTorr-(c)], (b) RF power [125 W-(d), 150 W-(e), and 175 W-(f)], and (c)**

**annealing [150 °C-(g), 200 °C-(h), and 250 °C-(i)] under vacuum environment.**

#### **4.3.6 Optical Transmittance And Urbach Energy**

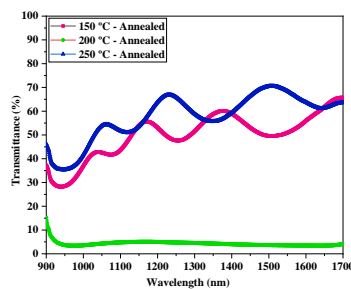
To acquire solar radiation from the atmosphere, bandgap energy ( $E_g$ ) of an absorber material should follow solar spectrum response AM 1.5 G. Number of generated charge carrier from solar photon with energy ( $E$ ) can be quantified by the bandgap  $E_g$  of an absorber material when  $E \geq E_g$ . Minimizing bandgap  $E_g$  will maximize the photon contribution to the short circuit density. According to the Shockley-Queisser theory, the collection probability for all photo-generated electrons- holes pair at the short circuit is unity. The maximum amount of short circuit current  $J_{sc}$  is a function of incoming photon flux  $\Phi_{inc}$  and absorbance  $A(E)$  not reflected or transmitted photon flux. The optical transmittance of CIGS thin film is shown in Fig. 4.8 (a, b, and c). Average optical transmittance for CIGS thin-film at different pressure is 38.03-60.85 % while for different RF power 42.68-60.85 % and 50.99-58.28 %. All CIGS thin films exhibit interference patterns that confirm the good uniformity of CIGS thin films [20]. Due to changes in the stoichiometric composition shift in transmittance maxima ( $T_{max}$ ) and transmittance minima ( $T_{min}$ ) was observed. Band tail was also present as there was no sharp fall at edges, confirming the presence of defects near absorbance band-edge. Among all, CIGS thin-film vacuum annealed at 200 °C has only 4.5 % of average transmittance. The bandgap energy ( $E_g$ ) of all CIGS thin film is dependent on stoichiometric composition especially Ga content. Reports have confirmed that tuning the bandgap between CIS and CGS, Ga content plays an important role. Using Tauc's equation, the plot of  $(\alpha h\nu)^2$  versus energy ( $E$ ) has been plotted to calculate the optical bandgap ( $E_g$ ) of all CIGS thin film as shown in Fig. 4.9. The bandgap of CIGS thin-film deposited at various conditions varies between 1.09-1.28 eV. From Fig. 4.10 (a), it is deduced that the shift in bandgap is a function of change in Ga content. For Ga = 0.3 % the theoretical optical bandgap should be 1.15 eV. But due to variation in Ga content, the bandgap varied. For CIGS thin film deposited at 15 mTorr and 150 W, the bandgap is nearly 1.10 eV having Ga nearly 0.3 %. Shift in optical bandgap also due to the formation of defects at the lattice sites. The

transmittance of CIGS thin-film vacuum annealed at 200 °C shows only 4.5 %, but Raman spectra reveal that instead of the chalcopyrite CIGS phase, metallic-selenide (CuSe or Cu<sub>2-x</sub>Se) has formed. Therefore, all CIS thin-film possess a bandtail near the excitonic absorption edge. This tail at the absorption band edge is due to the presence of defects in the thin films. Disorder in the structural and electronic properties may arise due to growth procedure, the impact of external temperature, phonons, presences of impurities, etc. This disorder is measured in terms of Urbach energy (E<sub>u</sub>) and the bandtail is termed as Urbach tail. An exponential decay below the absorption band edge is known as ‘sub-bandgap’. Plotting ln( $\alpha$ ) versus Energy (E), where  $\alpha$  is absorption coefficient, followed by linear fitting and finally inverse of the slope is the estimation of Urbach energy. More Urbach energy means a high order of defects. Urbach Energy for CIGS thin-film has been plotted in Fig. 4.10 (b). The lowest Urbach energy was noted for 15 mTorr is 0.30 meV. Exceptionally, for room temperature deposited and vacuum annealed CIGS thin-film at 250 °C has Urbach energy about 0.330 and 0.129 meV. This may be due to negligible binary compound CuSe or Cu<sub>2-x</sub>Se has formed so the degree of defects is much low compared to other deposition conditions.



(a)

(b)



(c)

**Fig. 4.8: Optical Transmittance of CIGS thin films deposited at different (a) pressure, (b) power, and (c) Annealing under vacuum environment.**

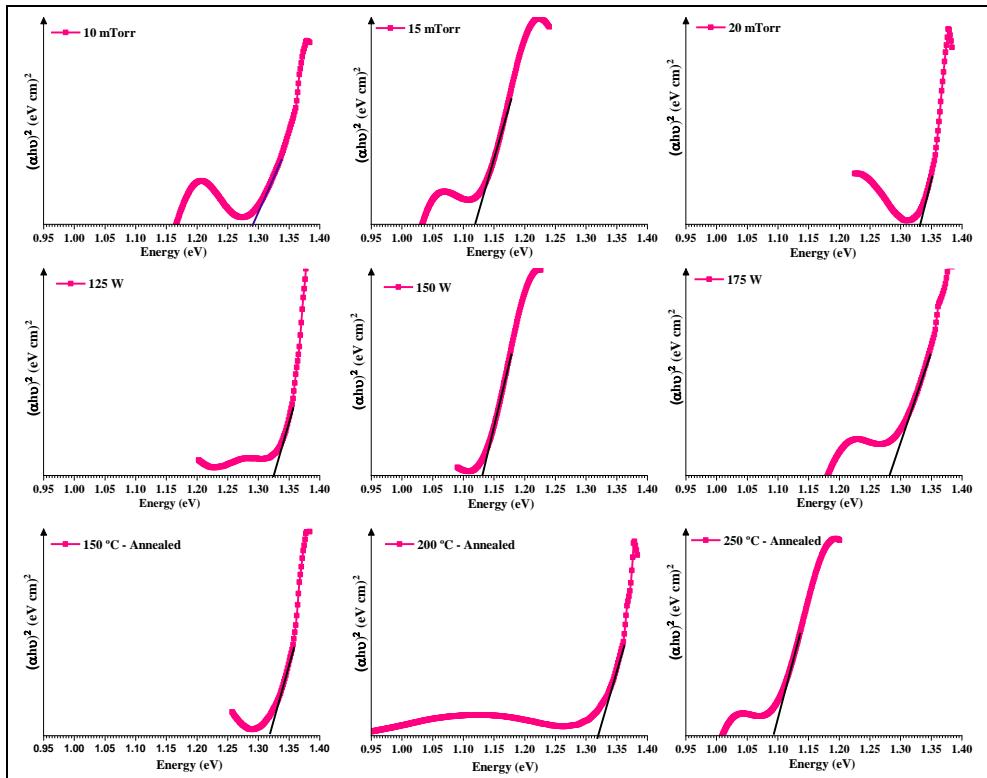


**Fig 4.9: Plot of  $(\alpha h\nu)^2$  versus energy (E) of CIGS thin films deposited at various deposition conditions.**

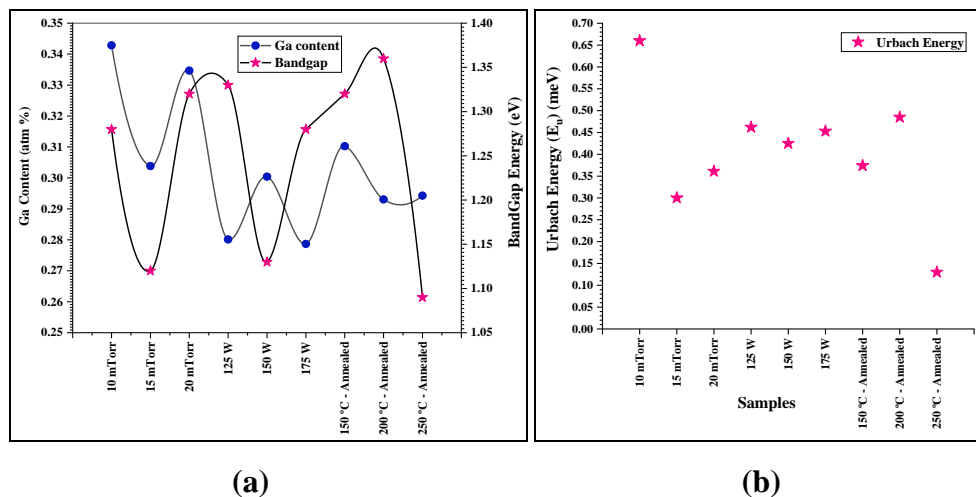


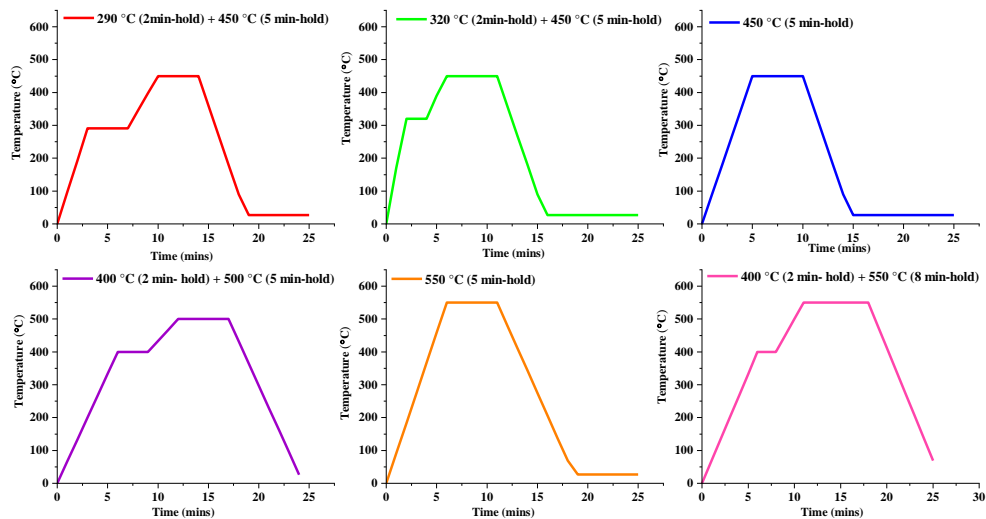
**Fig 4.10: (a) Dependence of Ga content on optical bandgap and (b) Urbach Energy of CIGS thin films deposited at various deposition conditions.**

#### 4.4 Consequences of Eclectic CIGS Annealing Profiles

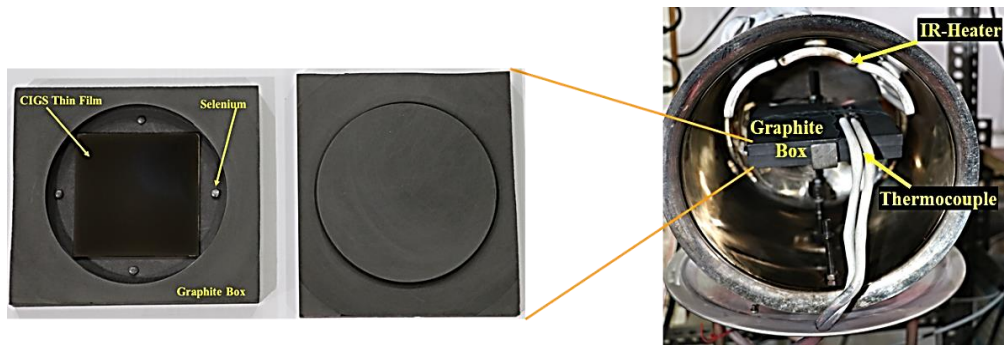
A chalcopyrite Copper Indium Gallium Diselenide (CIGS) possesses an intricate pseudobinary phase system. To evaluate the CIGS phase formation initially, annealing was carried out for one hour up to temperature 250 °C. As a result, the nanocrystalline chalcopyrite phase has formed with assorted binary and ternary phases. Therefore, another approach of rapid thermal annealing after the deposition of chalcopyrite via the RF-sputtering technique has been experimented [21]. The CIGS thin-film has been grown on soda-lime glass coated with Mo (SLG/Mo/CIGS). 0.04 gm selenium beads were added during each profile process. Schematic of annealing profile for RTA process has been plotted in Fig. 4.11(a). Rapid thermal Annealing process setup and graphite box containing sample and selenium are shown in Fig. 4.11(b) Six different annealing profiles mentioned in Table 4.2 were evaluated.

**Table 4.2: List of Annealing Profiles for CIGS phase formation.**

Sample	Profile
A	290 °C (2min-hold) + 450 °C (5 min-hold)
B	320 °C (2min-hold) + 450 °C (5 min-hold)
C	450 °C (5 min-hold)
D	400 °C (2 min- hold) + 500 °C (5 min- hold)
E	550 °C (5 min- hold)
F	400 °C (2 min- hold) + 550 °C (8 min- hold)



(a)



(b)

**Fig. 4.11: (a) Rapid Thermal Annealing (RTA) Profile for CIGS phase formation, (b) Rapid Thermal Annealing setup for the annealing process.**

#### 4.4.1 X-Ray Diffraction Analysis

X-ray diffraction of CIGS with six different rapid thermal annealing profiles has shown in Fig. 4.12. In Fig. 4.12 (a) annealing profile (A) does not possess preferential orientation growth of the CIGS phase. It has concocted binary  $\text{Cu}_2\text{Se}$  and ternary phase. Other phases such as  $\text{Cu}_m\text{In}_m$ ,  $\text{CISe}_2$ ,  $\text{In}_a\text{Se}_b$ , and  $\text{CuGa}_2$  may be convoluted. As the Mo/CIGS sample annealed as per profile (B), phases started deconvoluted. CIGS,  $\text{Cu}_2\text{Se}$ , and  $\text{MoSe}_2$  have been observed at  $2\theta$  values (112)  $26.02^\circ$ ,  $29.45^\circ$  (111), and  $31.45^\circ$  as shown in Fig. 4.12 (b). All phases actuate to transform from binary and ternary phases to the chalcopyrite phase. Increasing annealing ramp temperature to  $450^\circ\text{C}$ , promotes the preferential growth of the CIGS phase. Annealing profile (C) instigates the (112) CIGS at  $2\theta$  values (112)  $26.95^\circ$ , phase shown in Fig. 4.12 (c). Also, the negligibly  $\text{Cu}_2\text{Se}$  phase has decreased compared to profile (B). Further, the annealing profile has finely modulated. The intensity and sharpness of the CIGS phase improve along with preferential orientation at  $2\theta$  values (112)  $26.45^\circ$  shown in Fig. 4.12 (d). Still,  $\text{Cu}_2\text{Se}$  at  $2\theta$  values  $27.94^\circ$  intermixed with  $\text{CISe}_2$  phase is observed as an annealing process carried out according to profile (D). Profile (E) holds the SLG/Mo/CIGS for 5 mins at  $550^\circ\text{C}$  temperature; it intensifies the CIGS phase at  $2\theta$  values  $26.77^\circ$ .  $\text{Cu}_2\text{Se}$  phase starts reducing  $2\theta$  values  $27.85^\circ$ , whereas  $\text{CISe}_2$  phase almost disappeared as shown in Fig. 4.12 (e). Finally, under the annealing profile (F), refined phase (112) was observed at  $2\theta$  values  $27.19^\circ$  shown in Fig. 4.12 (f). No other phase except negligible

Cu<sub>2</sub>Se was observed. Of course, MoSe<sub>2</sub> and Mo appeared but less intense compared to other profiles due to large grain coverage at the surface [22, 23].

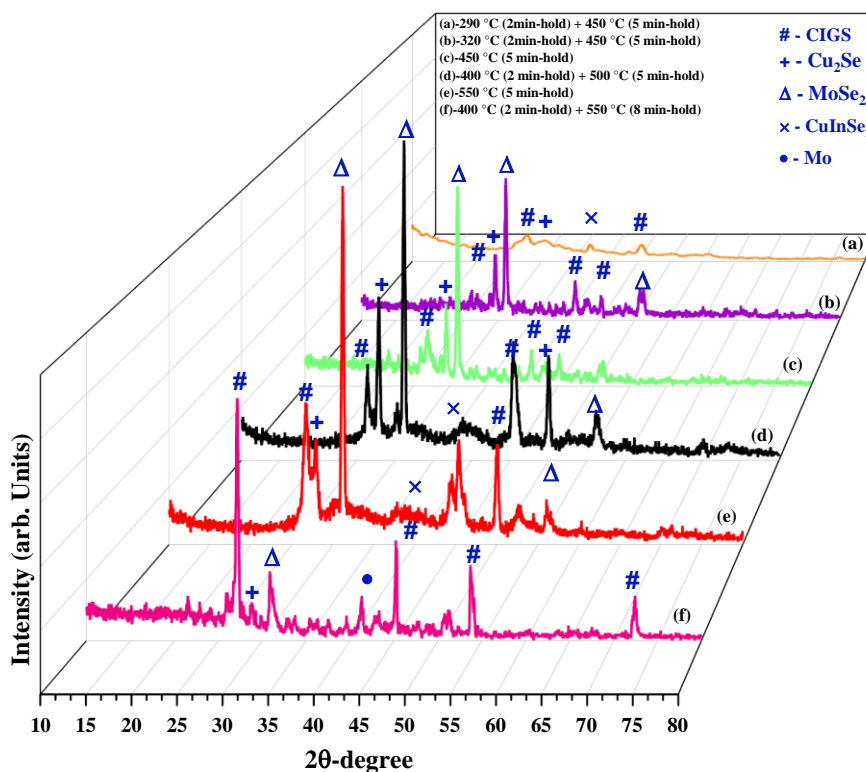
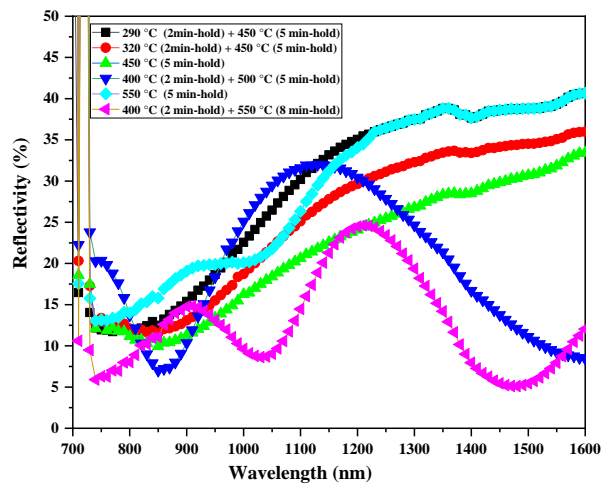


**Fig. 4.12: X-ray diffraction spectra of different Rapid Thermal Annealing (RTA) Profiles for SLG/Mo/CIGS phase formation.**

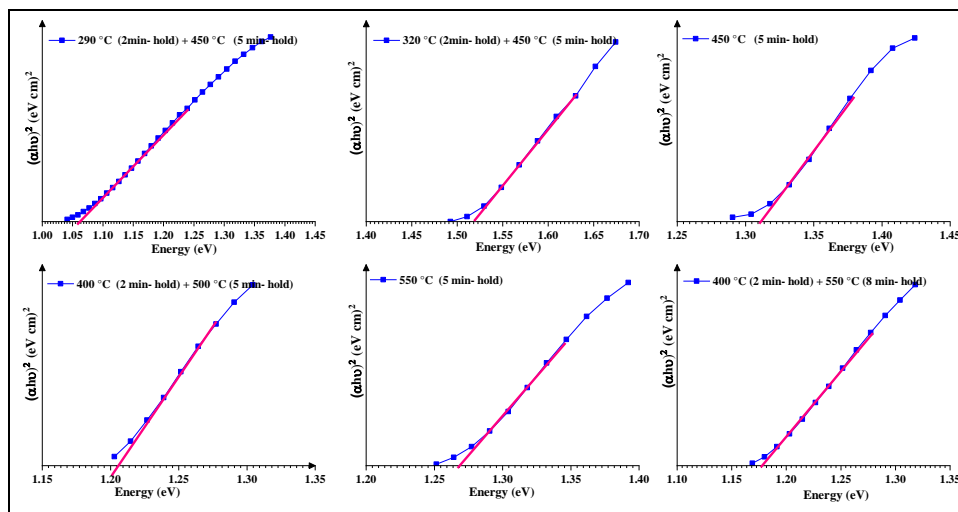
#### 4.4.2 Optical Reflectivity and Bandgap Analysis

The optical reflectivity of SLG/Mo/CIGS of all rapid thermal annealing process has been measured as shown in Fig. 4.13 (a). Optical reflectivity was average ranged between 24-42 %. Profile A, B, C, and E have absorption edge less than wavelength 800 nm. There is an increase in reflectivity with the increase in wavelength. Such increase in reflectivity with the absorption edge less than 800 nm is due to the presence of binary and ternary phases such as Cu<sub>2</sub>Se, CuSe, and few other metalloids. A constant increase in reflectivity is due to large grain formation at the surface. While profile D and F have absorption near 850 and 1040 nm. Also, profile (F) has a less intense absorption edge with a band tail at a wavelength less than 750 nm. This result can interfere as a mixture of majorly CIGS phase and minor binary phase Cu<sub>2</sub>Se. Fig. 4.13 (b) presents the optical bandgap of SLG/Mo/CIGS annealed profiles. Profile A has bandgap 1.05 eV due to off-stoichiometry and it leans toward the CuInSe<sub>2</sub> phase. Whereas profile

B possesses an increment in Ga content which increases the bandgap to 1.52 eV. Reduction in bandgap was observed in profile C. Single-step annealing under ramp temperature 450 °C compensates off-stoichiometry composition, but still, optimal bandgap deviates from the bulk. Tuning between CuInSe<sub>2</sub> and CuGaSe<sub>2</sub> phase occurs as a result of Ga rich phase has formed. Further, the D and E annealing profile reduces the secondary phase and transforms them into the chalcopyrite CIGS phase. The bandgap recorded was around 1.20 eV and 1.27 eV due to slightly more Ga content. Profile F possesses a bandgap near to 1.17 eV which is slightly deviated from the bulk composition. The spectral fringes were also observed in reflectivity spectra which confirms the uniformity of annealed SLG/Mo/CIGS thin-film. Profile F substantially assists the recrystallization and maintains the stoichiometry composition which results in the optical bandgap [24].



(a)



(b)

**Fig. 4.13: (a) Reflectivity X-ray spectra and (b) Optical Bandgap of different Rapid Thermal Annealing (RTA) Profiles for SLG/Mo/CIGS phase formation.**

### 4.4.3 Energy Dispersive X-ray Analysis

**Table 4.3: Elemental composition analysis of SLG/Mo/CIGS Annealing Profile.**

Profiles	Cu (at%)	In (at%)	Ga (at%)	Se (at%)	Cu/ (In+Ga)	Ga/ (In+Ga)	Se/ (Cu+In+Ga)
A	12.2	28.94	6.99	51.88	0.33	0.49	0.13
E	24.12	15.26	6.35	54.27	1.11	0.29	1.18
B	25.15	16.77	5.75	51.96	1.11	0.25	1.08
C	28.94	15.53	10.48	45.03	1.11	0.40	0.81
D	23.25	22.55	9.24	44.95	0.73	0.29	0.81
F	23.05	18.75	6.5	53.03	0.91	0.31	0.12

Compositional stichometry of annealed SLG/Mo/CIGS profile was estimated using the EDAX technique as shown in Table 4.3.  $\text{Cu}_{\text{poor}}$  and  $\text{In}_{\text{rich}}$  content were present under annealing profile A. off course several mixed binary, ternary, and metalloids have formed. At temperature 290 °C, Ga-rich also has formed; but due to high surface tension, the growth is moderate. Such phases have not been observed in XRD or Raman spectroscopy because the Ga rich phase is small in size are passivated by  $\text{Cu}_2\text{Se}$ ,  $\text{CuSe}$ , or  $\text{In}_2\text{Se}_3$ . Annealing under profile B, increase the Cu content and decrease the In content. A slight reduction in Ga content was also observed.  $\text{Cu}_{\text{rich}}$  and  $\text{In}_{\text{poor}}$  have formed at temperature 320 °C and further annealing at 450 °C does not result in pure CIGS phase formation. The off-stichometry composition was observed even when annealed under a single-step ramp temperature of 450 °C. Selenium content slightly decreases with an increase in In content.  $\text{Cu}_{\text{rich}}$  phases such as  $\text{Cu}_2\text{Se}$ ,  $\text{CuSe}$  may have formed. Besides, Se is also consumed in  $\text{MoSe}_2$  phase formation. The decrease in selenium content was found in profile D and E and meanwhile Ga content increased. Whereas in profile F compositional analysis, stichometry was

maintained with a slight deviation in Se/(Cu+In+Ga) ratio. The ratio is more than due to extra selenium added during the annealing process [25, 26].

#### 4.4.4 Raman Spectroscopic Analysis

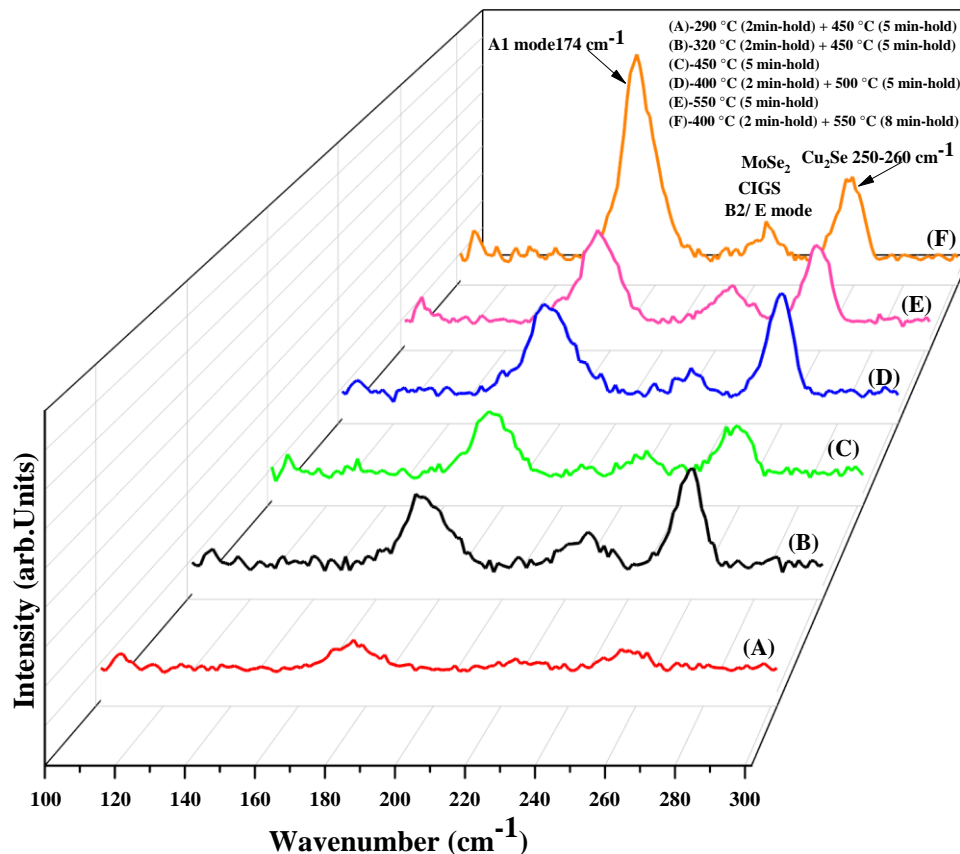


**Fig. 4.14: Raman Spectroscopic Analysis of different Rapid Thermal Annealing (RTA) Profiles for SLG/Mo/CIGS phase formation.**

Raman spectroscopy is the imprint of phase formation. Above Fig. 4.13 describes the Raman peak of the SLG/Mo/CIGS phase annealed under different annealed profiles. The intensity of the A1 mode peak under profile is not spectacular. Profile B, C, D, and E possess intense A1 mode peak to compare to profile A. 172, 227 cm<sup>-1</sup> peaks refer to A1 mode, B<sub>2</sub>/E mode of CIGS phase, and 259 cm<sup>-1</sup> peaks were observed under profile B which corresponds to Cu<sub>2</sub>Se phase. Similarly, for profile C peaks at 175 cm<sup>-1</sup>, 228 cm<sup>-1</sup>, and 258 cm<sup>-1</sup>; for profile D peaks at 173, 227, and 259 cm<sup>-1</sup>; for profile E peaks at 178, 226, and 257 cm<sup>-1</sup> and profile F peaks at 174, 224, and 259 cm<sup>-1</sup> was observed. All profiles except A possess intense A1 mode and B<sub>2</sub>/E mode of CIGS phase peaks.

These results are in agreement with XRD, and EDAX compositional analysis. MoSe<sub>2</sub> phase has been observed but it is not distinctly deconvoluted with the B<sub>2</sub>/E mode of the CIGS phase [27, 28].

## Conclusions

CIGS sputter targets were fabricated using cold press following the vacuum sintering process. CIGS thin-film layer deposited by RF sputtering technique at 15 mTorr deposition pressure, 150 W RF-power, and two-step rapid thermal annealing process is optimized for the formation of (112) phase. The elemental stoichiometry was maintained, where Ga/(In+Ga) is 0.31 and Cu/(In+Ga) is 0.91. This compositional stoichiometry is agreed upon for developing a highly efficient CIGS device. The optical analysis estimates the bandgap of the CIGS thin-film layer near 1.17 eV. The Raman spectroscopic analysis infers the presence of the CIGS phase A1 mode at 174 cm<sup>-1</sup> and B<sub>2</sub>/E mode at 224 cm<sup>-1</sup>.

## References

- [1] L. L. Kazmerski, F. R. White, and G. K. Morgan, *Applied Physics Letters*, **29** (4) (1976) 268-270.
- [2] W. E. Devaney, W. S. Chen, J. M. Stewart and R. A. Mickelsen, *IEEE Transactions on Electron Devices*, **37** (2) (1990) 428-433.
- [3] Martin Green, Ewan Dunlop, Jochen Hohl-Ebinger, Masahiro Yoshita, Nikos Kopidakis and Xiaojing Hao, *Progress in Photovoltaics*, Solar cell efficiency tables (version 57), (2020) 1-13.
- [4] F. Kessler, D. Hariskos, S. Spiering, E. Lotter, H. P. Huber and R. Wuerz, *High-Efficient Low-Cost Photovoltaics*, Springer Series in Optical Sciences Volume 140, **Chapter 9**, (2020) 175-208.
- [5] Xiaolong Li, Ming Zhao, Daming Zhuang, Mingjie Cao, Liangqi Ouyang, Li Guo Rujun Sun and Zedong Gao, *Vacuum*, **119**, (2015) 15-18.
- [6] C. Suryanarayana, E. Ivanov, R. Noufi, M. A. Contreras and J. J. Moore, *Thin Solid Films*, **332** (1998) 340-344.
- [7] Zhang Ning, Zhuang Da-Ming and Zhang Gong, *Materials Science and Engineering B*, **166** (2010) 34-40.

- [8] Leng Zhang, Daming Zhuang, Ming Zhao, Qianming Gong, Li Guo, Liangqi Ouyang, Rujun Sun, Yaowei Wei and Shilu Zhan, *Vacuum*, **137** (2017) 205-208.
- [9] Jason D. Myers, Jesse A. Frantz, Robel Y. Bekele, Vinh Q. Nguyen, and Jas S. Sanghera, *Proc. of SPIE*. **9177** (2014) 917708-1-917708-7.
- [10] Jiang Liu, Daming Zhuang, Hexin Luan, Mingjie Cao, Min Xie and Xiaolong Li, *Progress in Natural Science: Materials International* **23** (2) (2013) 133-138.
- [11] Gang Shi and Junhao Chu, *Proc. of SPIE*, **7995** (2011) 79950A-1-79950A-4.
- [12] Tae Won Kim, Young Baek Kim, Sang In Song, Chae Whan Jung and Jong Ho Lee, *Proc. of SPIE*, **8110** (2011) 811008-1-811008-6.
- [13] Jae Cheol Park, Mowafak Al-Jassim, Seung Wook Shin, Jin Hyeok Kim and Tae Won Kim, *Ceramics International*, **45** (2019) 4424-4430.
- [14] C. M. Ruiz, X. Fontané, A. Fairbrother, V. Izquierdo-Roca, C. Broussillou, S. Bodnar, A. Pérez-Rodríguez, and V. Bermúdez, *Applied Physics Letters* **102**, (2013) 091106-1-091106-4.
- [15] A. J. Zhou, D. Mei, X. G. Kong, X. H. Xu, L. D. Feng, X. Y. Dai, T. Gao and J. Z. Li, *Thin Solid Films*, **520** (2012) 6068-6074.
- [16] S. Roy, P. Guha, S. N. Kundu, H. Hanzawa, S. Chaudhuri and A. K. Pal, *Materials Chemistry and Physics*, **73** (2002) 24–30.
- [17] Y. C. Lin, Z. Q. Lin, C. H. Shen, L. Q. Wang, C. T. Ha and Chris Peng, *J Mater Sci: Mater Electron*, **23** (2012) 493-500.
- [18] Jing Tian, Lianqin Peng, Jinwei Chen, Gang Wang, Xueqin Wang, Hong Kang and Ruilin Wang, *Appl. Phys. A*, **116** (2014) 1813-1820.
- [19] A. J. Zhou, D. Mei, X. G. Kong, X. H. Xu, L. D. Feng, X. Y. Dai, T. Gao and J. Z. Li, *Thin Solid Films*, (2012) 6068-6074.
- [20] Jae-Cheol Park, Mowafak Al-Jassim, Byung-Teak Lee and Tae-Won Kim, *Journal of Alloys and Compounds*, **812** (2020) 152065-1-6.
- [21] Xuege Wang, Sheng S. Li, W. K. Kim, S. Yoon, V. Craciun, J. M. Howard, S. Easwaran, O. Manasreh, O. D. Crisalle and T. J. Anderson, *Solar Energy Materials & Solar Cells*, **90** (2006) 2855-2866.

- [22] Liangqi Ouyang, Daming Zhuang, Ming Zhao, Ning Zhang, Xiaolong Li, Li Guo, Rujun Sun and Mingjie Cao, *Phys. Status Solidi A*, **1-5** (2015) 1-5.
- [23] J. H. Shi, Z. Q. Li, D. W. Zhang, Q. Q. Liu and S. M. Huang, *Progress in Photovoltaics: Research and Applications*, **19 (2)** (2011) 160-164.
- [24] Jae-Cheol Park, Jeon-Ryang Lee, Mowafak Al-Jassim, and Tae-Won Kim, *Optical Materials Express*, **11** (2016) 3541-3549.
- [25] Lei Sun, Jianhua Ma, Nianguan Yao, Zhiming Huang & Junhao Chu, *J Mater Sci: Mater Electron*, **27** (2016) 9124-9130.
- [26] Yong Yan, Shasha Li, Yufeng Ou, Yaxin Ji, Chuanpeng Yan, Lian Liu, Zhou Yu and Yong Zhao, *J. Mod. Transport*, **22** (2014) 37-44.
- [27] Wolfram Witte, Robert Kniese and Michael Powalla, *Thin Solid Films*, **517** (2008) 867-869.
- [28] L. Minkevičius, S. Balakauskas, M. Šoliūnas, R. Suzanovičienė, J. Uzėla, G. Molis, R. Juškėnas, A. Selskis, G. Niaura, G. Valušis and V. Tamošiūnas, *Lithuanian Journal of Physics*, **53 (4)** (2013) 219-226.